# Chapter 2

# Magnet system and magnetic field

This chapter begins with a brief description of the ATLAS magnet system (section 2.1), which consists of one solenoid and three toroids (one barrel and two end-caps). Section 2.2 proceeds with a description of the current understanding of the magnetic field across the whole apparatus. This includes mapping of the solenoid field and first measurements of the barrel toroid field with the Hall-probe system, as well as calculations to determine the detailed field map with the required accuracy and performance specifications to be used in ATLAS simulation and reconstruction applications.

## 2.1 Magnet system

ATLAS features a unique hybrid system of four large superconducting magnets. This magnetic system is 22 m in diameter and 26 m in length, with a stored energy of 1.6 GJ. After approximately 15 years of design, construction in industry, and system integration at CERN, the system is installed and operational in the underground cavern. This section presents the properties of the magnets and their related services. More details can be found in [2] for the solenoid.

Figure 1.1 shows the general layout, the four main layers of detectors and the four superconducting magnets which provide the magnetic field over a volume of approximately 12,000 m$^3$ (defined as the region in which the field exceeds 50 mT). The spatial arrangement of the coil windings is shown in figure 2.1. The ATLAS magnet system, whose main parameters are listed in table 2.1, consists of:

- a solenoid (section 2.1.1), which is aligned on the beam axis and provides a 2 T axial magnetic field for the inner detector, while minimising the radiative thickness in front of the barrel electromagnetic calorimeter;
- a barrel toroid (section 2.1.2) and two end-cap toroids (section 2.1.3), which produce a toroidal magnetic field of approximately 0.5 T and 1 T for the muon detectors in the central and end-cap regions, respectively.

The first conceptual design of the magnet system was sketched in the early 1990's, and the technical design reports [3–6] were published in 1997. Regular project overviews and status reports of design and production were made available [7, 8] throughout the design and manufacturing

2008 JINST 3 S08003

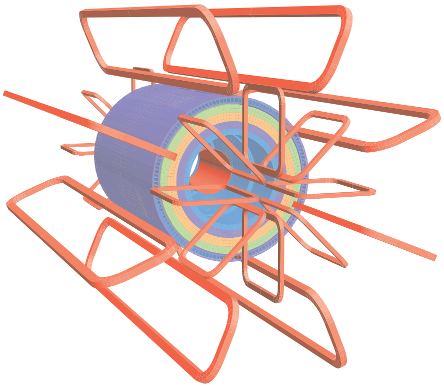

**Figure 2.1**: Geometry of magnet windings and tile calorimeter steel. The eight barrel toroid coils, with the end-cap coils interleaved are visible. The solenoid winding lies inside the calorimeter volume. The tile calorimeter is modelled (section 2.2.2) by four layers with different magnetic properties, plus an outside return yoke. For the sake of clarity the forward shielding disk (section 3.2) is not displayed.

**Figure 2.2**: Bare central solenoid in the factory after completion of the coil winding.

2008 JINST 3 S08003

phases. The cold-mass and cryostat integration work began in 2001. The first barrel toroid coil was lowered in the cavern in fall 2004, immediately followed by the solenoid (embedded inside the LAr barrel calorimeter). The remaining seven barrel-toroid coils were installed in 2004 and 2005, and the end-cap toroids in the summer of 2007.

### 2.1.1 Central solenoid

The central solenoid [2] is displayed in figure 2.2, and its main parameters are listed in table 2.1. It is designed to provide a 2 T axial field (1.998 T at the magnet's centre at the nominal 7.730 kA operational current). To achieve the desired calorimeter performance, the layout was carefully optimised to keep the material thickness in front of the calorimeter as low as possible, resulting in the solenoid assembly contributing a total of $\sim$ 0.66 radiation lengths [9] at normal incidence. This required, in particular, that the solenoid windings and LAr calorimeter share a common vacuum vessel, thereby eliminating two vacuum walls. An additional heat shield consisting of 2 mm thick aluminium panels is installed between the solenoid and the inner wall of the cryostat. The single-layer coil is wound with a high-strength Al-stabilised NbTi conductor, specially developed to achieve a high field while optimising thickness, inside a 12 mm thick Al 5083 support cylinder. The inner and outer diameters of the solenoid are 2.46 m and 2.56 m and its axial length is 5.8 m. The coil mass is 5.4 tonnes and the stored energy is 40 MJ. The stored-energy-to-mass ratio of only 7.4 kJ/kg at nominal field [2] clearly demonstrates successful compliance with the design requirement of an extremely light-weight structure. The flux is returned by the steel of the ATLAS hadronic calorimeter and its girder structure (see figure 2.1). The solenoid is charged and discharged in about 30 minutes. In the case of a quench, the stored energy is absorbed by the enthalpy of the cold mass which raises the cold mass temperature to a safe value of 120 K maximum. Re-cooling to 4.5 K is achieved within one day.

Table 2.1: Main parameters of the ATLAS magnet system.

| Property | Feature | Unit | Solenoid | Barrel toroid | End-cap toroids |
|---|---|---|---|---|---|
| **Size** | Inner diameter | m | 2.46 | 9.4 | 1.65 |
| | Outer diameter | m | 2.56 | 20.1 | 10.7 |
| | Axial length | m | 5.8 | 25.3 | 5.0 |
| | Number of coils | | 1 | 8 | $2 \times 8$ |
| **Mass** | Conductor | t | 3.8 | 118 | $2 \times 20.5$ |
| | Cold mass | t | 5.4 | 370 | $2 \times 140$ |
| | Total assembly | t | 5.7 | 830 | 2 x 239 |
| **Coils** | Turns per coil | | 1154 | 120 | 116 |
| | Nominal current | kA | 7.73 | 20.5 | 20.5 |
| | Magnet stored energy | GJ | 0.04 | 1.08 | 2 x 0.25 |
| | Peak field in the windings | T | 2.6 | 3.9 | 4.1 |
| | Field range in the bore | T | 0.9–2.0 | 0.2–2.5 | 0.2–3.5 |
| **Conductor** | Overall size | $mm^2$ | 30 x 4.25 | 57 x 12 | 41 x 12 |
| | Ratio Al:Cu:NbTi | | 15.6:0.9:1 | 28:1.3:1 | 19:1.3:1 |
| | Number of strands (NbTi) | | 12 | 38–40 | 40 |
| | Strand diameter (NbTi) | mm | 1.22 | 1.3 | 1.3 |
| | Critical current (at 5 T and 4.2 K) | kA | 20.4 | 58 | 60 |
| | Operating/critical-current ratio at 4.5 K | % | 20 | 30 | 30 |
| | Residual resistivity ratio (RRR) for Al | | $> 500$ | $> 800$ | $> 800$ |
| | Temperature margin | K | 2.7 | 1.9 | 1.9 |
| | Number of units $\times$ length | m | $4 \times 2290$ | $8 \times 4 \times 1730$ | $2 \times 8 \times 2 \times 800$ |
| | Total length (produced) | km | 10 | 56 | 2 x 13 |
| **Heat load** | At 4.5 K | W | 130 | 990 | 330 |
| | At 60–80 K | kW | 0.5 | 7.4 | 1.7 |
| | Liquid helium mass flow | g/s | 7 | 410 | 280 |

The electromagnetic forces are counteracted by the combination of the coil and warm-to-cold mechanical support, which maintains the concentricity of the windings. All solenoid services pass through an S-shaped chimney at the top of the cryostat, routing the service lines to the corresponding control dewar (section 2.1.4.2).

The coil was manufactured and pre-tested in the factory [10], came to CERN for integration in the LAr cryostat, underwent an on-surface acceptance test in its semi-final configuration [11], and was installed in its final central position in ATLAS in October 2005. The one week cool-down and a commissioning test up to nominal field were successfully completed in the summer of 2006 [12]. The solenoid is now ready for detector operation.

### 2.1.2 Barrel toroid

The main parameters of the magnet are listed in table 2.1. The cylindrical volume surrounding the calorimeters and both end-cap toroids (see figure 1.1) is filled by the magnetic field of the barrel toroid, which consists of eight coils encased in individual racetrack-shaped, stainless-steel vacuum vessels (see figure 2.3). The coil assembly is supported by eight inner and eight outer rings of struts. The overall size of the barrel toroid system as installed is 25.3 m in length, with inner and outer diameters of 9.4 m and 20.1 m, respectively.

2008 JINST 3 S08003

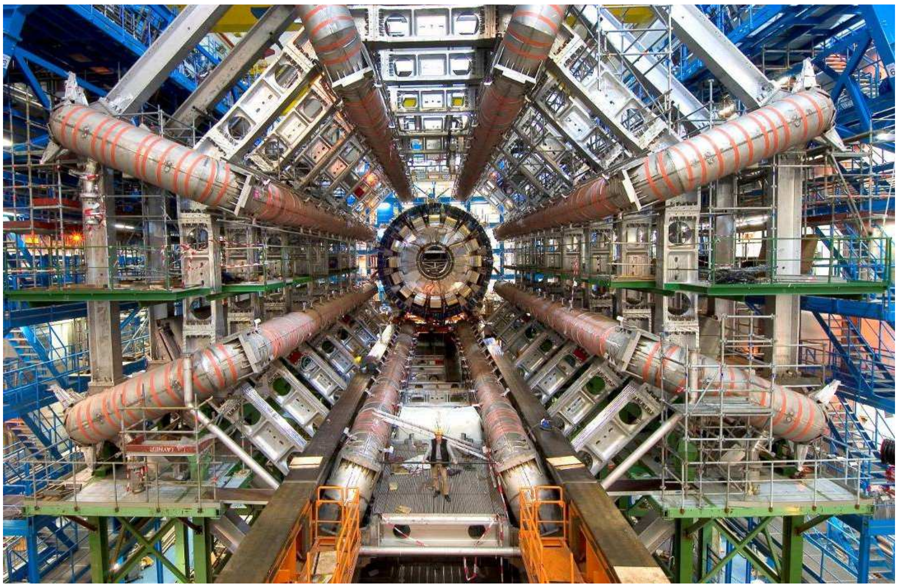

**Figure 2.3**: Barrel toroid as installed in the underground cavern; note the symmetry of the supporting structure. The temporary scaffolding and green platforms were removed once the installation was complete. The scale is indicated by the person standing in between the two bottom coils. Also visible are the stainless-steel rails carrying the barrel calorimeter with its embedded solenoid, which await translation towards their final position in the centre of the detector.

The conductor and coil-winding technology is essentially the same in the barrel and end-cap toroids; it is based on winding a pure Al-stabilised Nb/Ti/Cu conductor [13] into pancake-shaped coils, followed by vacuum impregnation.

The cold-mass integration [14] and the cryostat integration [15] were performed at CERN over a period of approximately three years, and were completed in summer 2005. In parallel, all coils successfully underwent on-surface acceptance test procedures [16]. Cool down and testing of the barrel toroid in the cavern took place in 2006. The cool down of the 360-tonne cold mass to 4.6 K takes five weeks. The test programme included normal ramps, up to nominal current (in 2 hours) followed by either a slow dump (in 2 hours) or a fast dump (in 2 minutes) in the case of a provoked quench. The ultimate test sequence that proved the system's health is shown in figure 2.4. The magnet current is raised in steps up to its nominal value of 20.5 kA and then finally up to 21.0 kA, demonstrating the ability of the system to withstand at least an additional 500 A. The current is then allowed to decay back to its design value; the magnet is finally turned off by a deliberate fast dump. After re-cooling the cycle was repeated, demonstrating that no degradation had occurred up to the nominal operating current. During a fast dump, triggered either manually or by the quench detection system, the stored energy of 1.1 GJ is absorbed by the enthalpy of the cold mass following the activation of four quench heaters per coil and in all eight coils, which forces the entire magnet into the normal conducting state within less than two seconds. This leads to a very safe global cold mass temperature of about 58 K and a hot-spot temperature in the windings of about 85 K maximum. The uniform quench heating system also ensures that the internal voltage in the toroid is kept at a low value of about 70 V. After a fast dump the magnet cooling system needs



2008 JINST 3 S08003

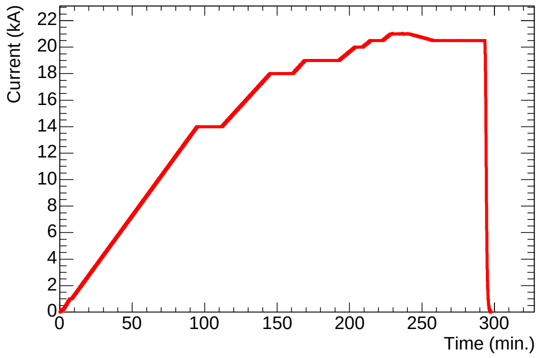


**Figure 2.4**: Time history of the barrel toroid current during an excitation test up to 102% of the nominal value. The current drops back to zero within two minutes of the deliberately-provoked quench.

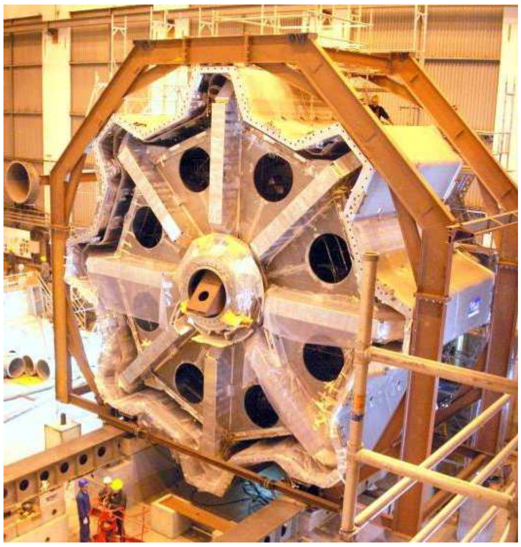

**Figure 2.5**: End-cap toroid cold mass inserted into the cryostat. The eight flat, square coil units and eight keystone wedges (with the circular holes) are visible.

about 50 hours to re-cool the toroid to 4.6 K whereafter normal operation can re-start. The details of the coil testing are published elsewhere, in [17] for the first coil, in [18] for an overall summary, and in [19] and [20] for quench behaviour and quench losses, respectively.

The net Lorentz forces of approximately 1400 tonnes per coil directed inwards and the self-weight of the toroids are counteracted by the warm structure of Al-alloy struts mounted in between the eight coils. However, the barrel toroid structure still deflects significantly under its own weight. After release of the temporary support structure and systematic loading of the toroid with its own weight of 830 tonnes and the additional 400 tonnes of weight of the muon chambers, the final shape of the toroid bore was designed to be cylindrical. The toroid coils were installed in calculated positions on an oval, longer by 30 mm in the vertical direction, to allow for structure deflection during load transfer from the temporary support structure. Since the release and removal of the installation supports, the upper edge of the toroid moved down by about 26 mm, which demonstrates that the design values had been well established and that the installation was precise to within a few millimetres.

The installation of the barrel toroid in the ATLAS cavern commenced in October 2004. It took about 11 months to install the complete toroid, as depicted in figure 2.3. This is discussed in more detail in section 9.6 within the context of the overall ATLAS installation, for which this toroid installation phase was one of the most demanding ones. The overall structure design and installation experience are reported in [21].

### 2.1.3 End-cap toroids

The main parameters of the two end-cap toroids are listed in table 2.1. These toroids generate the magnetic field required for optimising the bending power in the end-cap regions of the muon spectrometer system. They are supported off and can slide along the central rails, which facilitates the opening of the detector for access and maintenance (see section 9.5.1). Each end-cap toroid consists of a single cold mass built up from eight flat, square coil units and eight keystone wedges, bolted and glued together into a rigid structure to withstand the Lorentz forces (see figure 2.5). Design details are given elsewhere [22], and the production in industry of the coil modules and vacuum vessels is described in [23].

The cold masses were assembled and inserted into their cryostats at CERN. Figure 2.5 shows the first end-cap toroid interior just prior to the closing of the vacuum vessel. A crucial step in the integration process is the adjustment of the cold mass supports [24]. The weights of cold mass and vacuum vessel are 140 and 80 tonnes respectively. With the exception of windings, coil supports, and bore tube, the entire structure is made of Al alloy. With a weight of 240 tonnes, the end-cap toroids were some of the heaviest objects to be lowered into the cavern.

The end-cap-toroid cold masses will each be subject to a Lorentz force of 240 tonnes, pushing them against the stops mounted on the eight barrel toroid coils. Achieving the correct sharing of the forces in the axial tie-rods has therefore been a critical design goal. Prior to their installation in the cavern in summer 2007, both end-cap toroids passed tests at 80 K to check the magnet mechanics and electrical insulation after thermal shrinkage. Once the end-cap toroids are powered in series with the barrel toroid, the peak stress in the barrel-toroid windings, in the areas where the magnetic fields overlap, will increase by about 30%. After a four-week cooldown, both end-cap toroids were successfully tested at half current, albeit one at a time and in stand-alone mode. The final tests at full field will take place in the spring of 2008, after the installation of the shielding disks and with the end-cap calorimeters at their nominal position.

### 2.1.4 Magnet services

#### 2.1.4.1 Vacuum system

The insulating vacuum is achieved with diffusion pumps directly attached to the barrel and the end-cap toroids, two per coil for all toroids, each with a capacity of 3000 $m^3$/h. In addition, two roughing and three backing pumps are used in the low stray-field area at the cavern wall. Under normal conditions, with a leak rate less than $10^{-4}$ mbar · l/s, a single pump would be sufficient. However, for redundancy and in order to minimise detector down-time, extra pumping units were installed. Since the solenoid is installed inside the cryostat of the LAr barrel calorimeter, the insulation vacuum is controlled by the LAr cryogenic system (section 9.4.5) rather than by the magnet control system (see section 2.1.4.4).

#### 2.1.4.2 Cryogenics

The overall cryogenic systems in ATLAS are described in section 9.4. Here, details are provided on the system specific to the magnets.

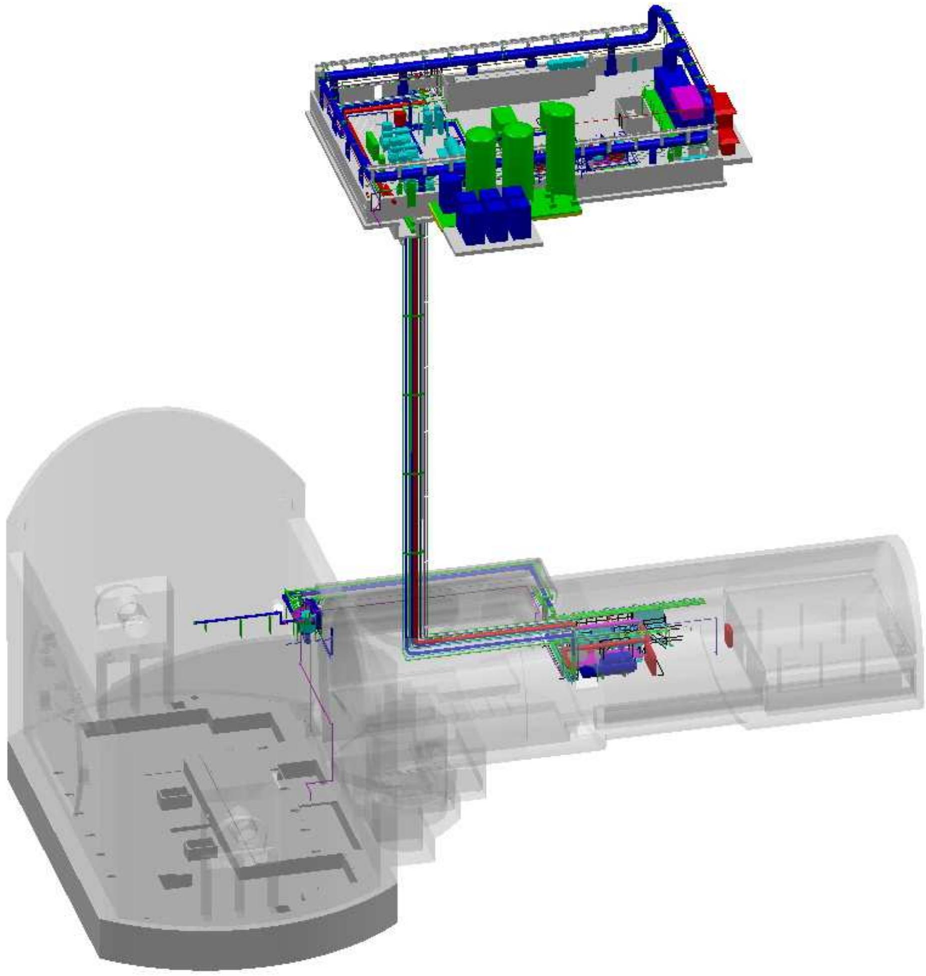

**Figure 2.6**: Layout of the magnet cryogenics system in the surface hall (compressors) and service cavern (shield refrigerator and helium liquefier). They deliver cold gas and liquid to the distribution valve box in the experimental cavern, from which the solenoid and the toroid proximity cryogenics are fed (see figure 2.7).

The overall magnet cryogenic system is divided into external, proximity, and internal cryogenics, which are connected via transfer lines. The lines serving the solenoid and barrel toroid remain fixed, whereas those of the end-cap toroids are partially flexible, as these toroids have to be moved to access the calorimeters and inner detector for maintenance and repairs (section 9.7).

The layout of the various cryogenic systems is shown in figure 2.6. The external cryogenics consist of two refrigerators (the main refrigerator and the shield refrigerator), a distribution transfer line, and a distribution valve box. The main refrigerator cold box has a refrigeration capacity of 6 kW at 4.5 K equivalent, while the shield refrigerator cold box has a refrigeration capacity of 20 kW at 40–80 K.

The gas buffers are located on the surface with the refrigerator compressors, while the refrigerator cold boxes are installed in the USA15 side cavern. The common distribution transfer line

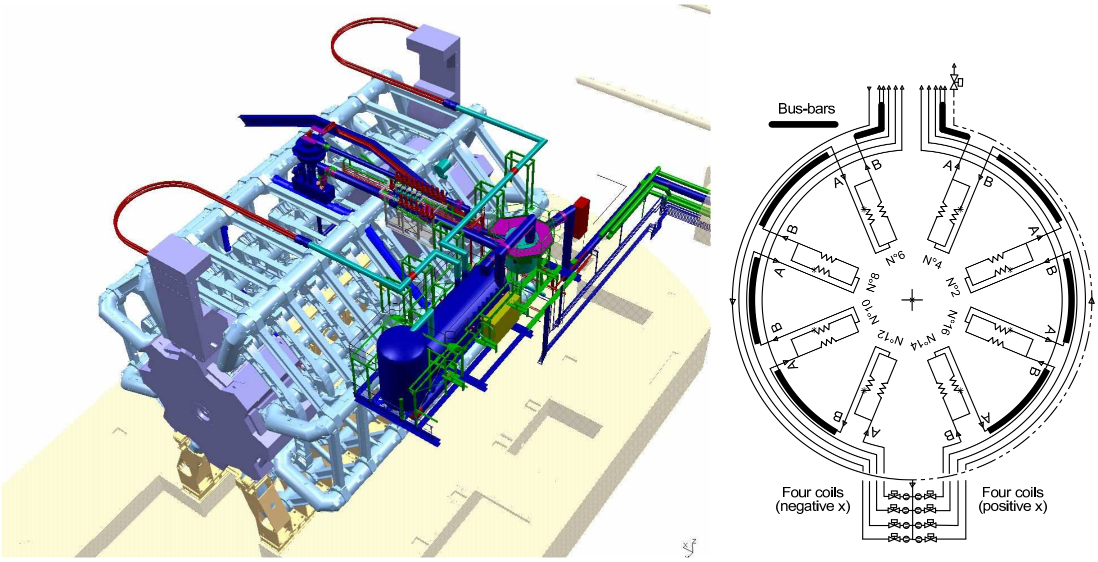


**Figure 2.7**: Left: Layout of underground service connections to the solenoid and toroid systems. The two large helium dewars can be seen on the side of the main cavern. Also shown are the fixed cryogenic lines supplying the solenoid and the cryo-ring for the barrel toroid coils at the top. The cryogenics lines in the flexible chains supply the two end-cap toroids and follow them whenever they move for detector access and maintenance. Right: schematic of the liquid-helium supply in the barrel toroid. The cryo-ring contains six standard sectors; a bottom sector with a valve box where the input flow per coil is measured and controlled; and the top sector where all lines come together and which is connected to the current lead cryostat.

makes the link to the distribution valve box in the main cavern. All proximity cryogenics equipment, including the storage dewar, cold pumps, cryostat phase separator, and distribution valve box (except for the valve unit of the solenoid) are positioned near the wall of the main cavern, as schematically shown in figure 2.7 (left).

The distribution valve box channels the fluids to two independent proximity cryogenic systems, one for the toroids (barrel cryo-ring and two end-caps) and one for the solenoid. For the toroids, there is a storage dewar with a capacity of 11,000 litres of liquid helium. There also exist a distribution valve box, a phase separator dewar with two centrifugal pumps and a storage capacity of 600 litres of liquid helium. The solenoid has a control dewar with a storage capacity of 250 litres of liquid helium, positioned at the top of the detector.

The proximity cryogenic equipment supplies coolant to the magnet internal cryogenics, which consist mainly of cooling pipes attached to the cold mass and the thermal shield. The aluminium cooling tubes are either welded to the outer surface of the Al-alloy support cylinder (solenoid) or embedded and glued inside and on top of the Al-alloy coil casings enclosing the pancake coils (toroids).

The toroids are cooled with a forced flow of boiling helium, which enters the magnets from the top. In the case of the barrel toroid (see figure 2.7), helium is supplied from the current lead cryostat positioned on the top sector, runs down to the distribution valve box at floor level with eight control valves regulating the flow in the eight coils, then goes up and enters the eight coils separately, while the return line returns to the top. A total of 1200 g/s of slightly sub-cooled liquid helium is circulated by means of centrifugal pumps, which take the liquid from the phase separator dewar. The system is equipped with two pumps for redundancy. The second pump is called into operation if the first one fails. The liquid helium in the storage dewar will be used in the event of a failure with the main refrigerator to provide the required cooling capacity to safely ramp down the toroids over a two-hour period.

The solenoid, with a cold mass of approximately five tonnes, is cooled by a direct Joule-Thompson flow from the main refrigerator and is slightly sub-cooled via a heat exchanger in the 250 litre helium control dewar.

The flow in the solenoid and the ten toroid cold masses is controlled individually to cope with variations in flow resistance and to guarantee helium quality in all coils. Given that the end-cap toroids and solenoid each have a single cold mass, there is a single flow control and the branches of cooling pipes (two for the solenoid and sixteen for each end-cap toroid) are arranged in parallel.

#### 2.1.4.3 Electrical circuits

The three toroids are connected in series to the 20.5 kA/16 V power supply shown schematically in figure 2.8 (left). They are however individually voltage-protected by the two diode/resistor ramp-down units. The electrical circuit of the central solenoid is similar and shown in figure 2.8 (right). It has a 8 kA/8 V power supply. The power supply, switches, and diode/resistor units are located in the side cavern and approximately 200 m of aluminium bus-bars provide the connections to the magnets in the cavern. Ramping up is accomplished at a rate of 3 A/s, leading to a maximum ramp-up time of two hours. In the case of a slow dump, the magnets are de-energised across the diode/resistor units in about 2.5 hours. Quench detection is by classical bridge connections across the entire barrel toroid, across the end-cap toroids and across the solenoid, as well as across individual coils, using differential voltage measurements with inductive voltage compensation.

There is a six-fold redundancy in the toroid quench detection grouped in two physically-separated units and cable routings. Quench protection is arranged by firing heaters in all toroid coils so that a uniform distribution of the cold-mass heating is achieved. Given the normal-zone propagation of 10–15 m/s, a toroid coil is switched back to the normal state within 1–2 seconds. As for the quench detection, the quench-protection heater circuits including power supply, cabling, and heaters embody a two-fold redundancy. A similar system is used for the solenoid. An overview of the magnet services can be found in [25].

#### 2.1.4.4 Magnet controls

A magnet control system steers and executes automatically the various running modes of the magnet system. Its implementation is realised as part of the overall ATLAS detector control system, as described in section 8.5. The hardware designs rely on a three-layer model, using distributed input/output connected via field-networks or directly by wiring to a process-control layer, the last layer being the supervisor.

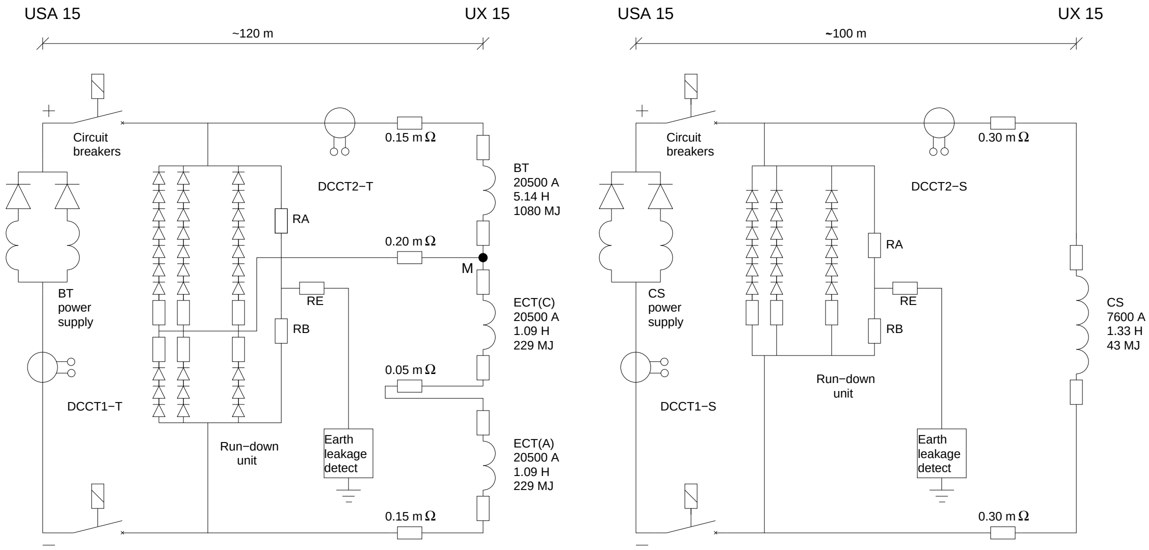


**Figure 2.8**: Electrical circuit showing the barrel (BT) and end-cap (ECT) toroids connected in series, fed by a 20.5 kA power converter and protected by a voltage-limiting diode/resistor ramp-down unit (left). Electrical circuit of the central solenoid (CS), fed by a 8 kA power converter (right).

The main control functions are:

- performing automatic operational sequences on a given magnet (sub-system tests);
- providing a communication interface with the power converter;
- regulating the helium flow in the magnet current leads as a function of the magnet current;
- enabling information exchange between the control system and other sub-systems such as vacuum or cryogenics;
- monitoring of all critical parameters in the coil (temperatures, strain and displacement gauges);
- performing calculations of non-linear sensor corrections (temperature sensors, vacuum gauges).

The supervision system displays a synopsis of the main process parameters, communicates with the power supply, collects both continuous and transient data, allows visualisation of any collected data on trend charts and archives collected data. For long-term storage and for correlation of data between different systems, a central data-logging system will regularly receive a pre-defined number of data items from each magnet system. A subset of the main control parameters is sent to the ATLAS detector safety system and also to the LHC machine (see section 9.10).

## 2.2 Magnetic field determination

The specifications on the determination of the magnetic field (section 2.2.1) are rather different in the inner detector (ID) and the muon spectrometer. In the ID cavity, the driving consideration is the absolute accuracy of the momentum scale. In the muon spectrometer, the field is highly non-uniform: residual bending-power uncertainties, if large enough, would translate primarily into degraded muon momentum resolution. Detailed magnetic modelling (section 2.2.2) and novel instrumentation (section 2.2.3) have allowed a high-precision mapping of the solenoid field (section 2.2.4) as well as a preliminary experimental validation of the field measurement and reconstruction strategy in the muon spectrometer (section 2.2.5). Studies are in progress to combine magnetic models with field measurements into an overall field map for ATLAS data-taking (section 2.2.6).

### 2.2.1 Performance specifications and measurement concepts

In the inner detector, the systematic error affecting the momentum measurement of charged tracks is dominated by the relative alignment of detector components and by bending-power uncertainties, the former being the more demanding. A high-precision measurement of the $W$-boson mass is clearly the most challenging goal for such measurements: a lepton from $W$ decay carries typically a transverse momentum of 40 GeV, resulting in a sagitta of approximately 1 mm as the lepton traverses the ID cavity. The systematic alignment uncertainties in the ID are unlikely to improve beyond the 1 $\mu$m level or 0.1% of the sagitta. This suggests setting a target of $\sim 5 \times 10^{-4}$ for the fractional bending power uncertainty, so that it remains negligible in the determination of the absolute momentum scale. Such stringent requirements can only be achieved reliably by in-situ mapping, using dedicated instrumentation inside the ID cavity, with all the relevant magnetic materials in place and just before the final installation of the ID itself. Eventual long-term drifts of the absolute scale will be detected to a much higher accuracy using permanently installed NMR probes.

In the muon spectrometer, the expected sagitta is approximately 0.5 mm for a muon with a momentum of 1 TeV. The extraction of the momentum from the Monitored Drift Tube (MDT) chamber measurements requires a precise knowledge of the field integral between consecutive chambers along the muon trajectory. Because the field gradient can reach 1 mT/mm, local bending-power uncertainties translate into fluctuations of the momentum scale from one region in space to another, adding in quadrature to the overall momentum resolution. In addition, the interpretation, in terms of spatial coordinates, of the drift time measured in the MDT's is sensitive to the local electric and magnetic fields experienced by the ionisation electrons in each tube. The corresponding functional requirements are extensively discussed in [26] and summarised in table 2.2.

For a given muon trajectory, three sources of uncertainty affect the measured curvature: field measurement errors; accuracy on the relative position of muon chambers and magnet coils; and trajectory measurement errors, in particular along the direction of MDT wires. For the purpose of setting specifications, it has been required (somewhat arbitrarily) that the combined effect of these sources degrade the momentum resolution by no more than 5% in relative terms; each source should then contribute no more than $\sim$3% of fractional resolution degradation, anywhere in the spectrometer volume.

**Table 2.2**: Summary of magnetic-field-related performance specifications in the muon spectrometer. The quoted spread reflects the $\eta - \phi$ variations in field gradient and/or strength.

| **Criterion** | **Bending-power accuracy** | **MDT drift properties** |
|---|---|---|
| Performance | $\Delta\sigma_{p_T}/\sigma_{p_T} < 5\%$ overall | Single-wire resolution degraded by $< 5\%$ |
| Field measurement accuracy | $\Delta B_\phi / B_\phi < 2-5 \times 10^{-3}$ | $\Delta B_{x,y,z} < 4$ mT (relative over chamber) |
| Reconstructed position of toroid conductors with respect to MDT tower | $\Delta R \sim 1-12$ mm, $R\Delta\phi \sim 1-6$ mm, $\Delta z \sim 2-30$ mm | - |
| Muon chamber 2nd-coordinate resolution | 1.7–5.5 mm | 6 to $\sim 100$ mm |

In-situ mapping of the spectrometer by conventional techniques would have been impractical because of the rapidly-varying field and very large volume. Instead, the muon system is equipped with a total of approximately 1840 B-field sensors; their readings are compared with magnetic simulations and used for reconstructing the field in space. This strategy was shown [27] to meet the field-map specifications above, provided the B-sensor readings, after correcting for perturbations induced by magnetic materials, are accurate to $\sim 1$ mT (absolute) and the field direction is measured to within $\pm$ 3 mrad.

### 2.2.2 B-field modelling

The total field in the ID cavity, the calorimeters, and the muon spectrometer is computed as the superposition of the Biot-Savart contributions of all magnet windings (see figure 2.1) with those of the magnetised calorimeter and with the localised perturbations induced by other ferromagnetic structures. In order to reach the required accuracy, the calculation combines numerical integration of the contributions of the solenoid, barrel-toroid and end-cap-toroid windings with finite-element modelling of magnetic structures.

The solenoid conductor model is described in section 2.2.4. The magnetised steel (tile calorimeter and solenoid flux-return girder), which surrounds the ID cavity, is predicted to modify the field by 4.1% at the geometrical centre of the coil. At nominal current, the total measured field is 1.998 T at the interaction point, and drops steeply from $\sim$ 1.8 T at $z = 1.7$ m to $\sim$ 0.9 T at the end of the ID cavity (see figure 2.9).

The toroid windings are, at this stage, described using their nominal geometry. The mesh density of the stored field map is tailored to the local field gradient to ensure an accurate representation of field variations (as also done for the solenoid). Depending on the radius $R$ and azimuth $\phi$, the field varies from 0.15 T to 2.5 T, with an average value of 0.5 T, in the barrel region, and from 0.2 to 3.5 T in the end-cap region [28]. The analysing performance of the toroid system can be roughly quantified by the field integral experienced by particles originating from the interaction point and propagating in a straight line (the ultimate criterion is the momentum resolution: a zero field integral does not necessarily imply infinite resolution). This available bending power is shown in figure 2.10 as a function of $|\eta|$. It shows good magnetic field coverage up to $|\eta| \sim 2.6$. The regions with low field integral, between $|\eta|$ = 1.4 and $|\eta|$ = 1.6, correspond to trajectories in the plane of an end-cap coil or of a barrel coil, where the fringe field of one magnet largely cancels the bending power of the other.

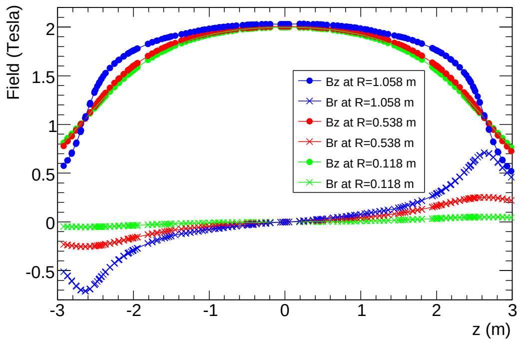


**Figure 2.9**: R- and z-dependence of the radial (Br) and axial (Bz) magnetic field components in the inner detector cavity, at fixed azimuth. The symbols denote the measured axial and radial field components and the lines are the result of the fit described in section 2.2.4.

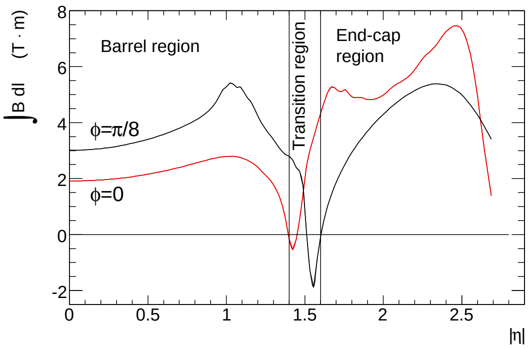


**Figure 2.10**: Predicted field integral as a function of $|\eta|$ from the innermost to the outermost MDT layer in one toroid octant, for infinite-momentum muons. The curves correspond to the azimuthal angles $\phi = 0$ (red) and $\phi = \pi/8$ (black).

A number of large magnetisable components, shown schematically in figure 2.11, distort the Biot-Savart field at different levels. Although amenable to experimental spot-checks (section 2.2.5), such perturbations can only be determined using field simulations.

The highly anisotropic structure of the tile calorimeter cannot be satisfactorily modelled using only a scalar permeability and an effective steel-packing factor: a formalism incorporating a magnetic permeability tensor, as well as a more sophisticated treatment of magnetic discontinuities at material boundaries, is called for. The problem is compounded by the superposition of the solenoid and toroid fields in the partially-saturated flux-return girder and in the tile calorimeter itself. A novel approach to magnetic-field modelling in such structures has therefore been developed and implemented in the B-field simulation package ATLM [29]. This package, which incorporates a careful description of the toroid and solenoid conductors as well as a detailed mathematical model of the tile calorimeter, is used both to compute the Biot-Savart field by numerical integration (as described above), and to predict, by a finite-element method, the field distortions caused by the tile calorimeter, the flux-return girder and the shielding disk in both the ID cavity and the muon spectrometer. Altogether, these distortions affect the field integral in the muon spectrometer by up to 4%, depending on $|\eta|$ and $\phi$; in addition, they induce, at the level of the inner MDT layers, local field distortions of up to $|\Delta\mathbf{B}| \sim 0.2$ T.

A few discrete magnetic structures, either inside the muon spectrometer or close to its outer layers, induce additional, localised magnetic perturbations. Their impact has been evaluated using the 3D finite-element magnetostatics package TOSCA [30]. The largest perturbations are caused by the air pads, jacks and traction cylinders which allow the calorimeters, the shielding disks, and the end-cap toroids to slide along the rails. These affect primarily the field distribution across the innermost MDT chambers in the lowest barrel sectors (BIL and BIS in sectors 12 to 14, see figures 2.11 and 6.1), and in addition impact the field integral at the level of up to 10% over small islands in $\eta - \phi$ space.

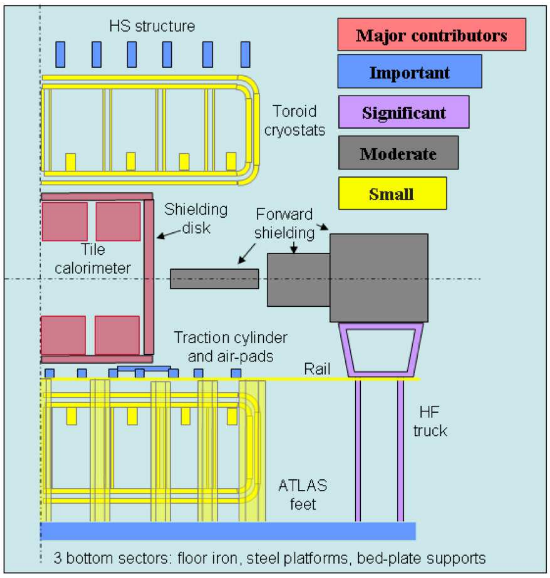


**Figure 2.11**: Sources of magnetic perturbations induced by metallic structures in or near the muon spectrometer.

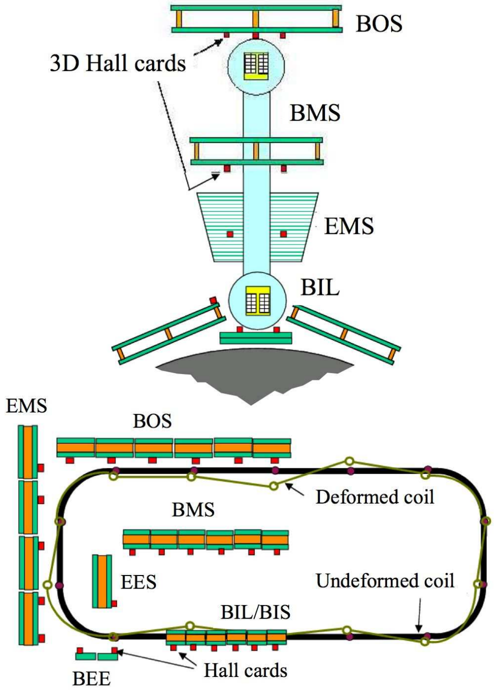


**Figure 2.12**: Schematic representation of the magnetic-sensor layout and coil deformation model, used to reconstruct the magnetic field inside a barrel octant. The MDT nomenclature is defined in tables 6.3 and 6.4 (see section 6.3).

The field perturbations caused in the outside MDT layers by the massive steel frame and platforms (HS structure described in section 9.5), which surround the detector, range from $|\Delta\mathbf{B}| \sim$ 2 mT up to $\sim$ 50 mT and rapidly decrease as one moves inwards from the outer to the middle chamber layer. While their impact on B-sensor readings and MDT drift properties does need to be taken into account, they barely affect the bending power, except possibly in a few narrow regions.

The other components in figure 2.11 have much less of an impact because either they lie in a low-field region, they intercept a very small fraction of the end-cap muons, or they are made of stainless steel with a high-field relative permeability very close to 1.

### 2.2.3 Magnetic field instrumentation and reconstruction

#### 2.2.3.1 B-field sensors

The inner detector is equipped with four NMR probes fixed to the wall of the inner warm vessel near $z \sim 0$ and equally spaced in azimuth. These probes measure the field strength with an accuracy of around 0.01 mT and will remain in place to monitor the ID field strength throughout the lifetime of ATLAS.

Because NMR probes only measure $|\mathbf{B}|$ and because they cease functioning in a gradient of a few tenths of mT/cm, the solenoid mapper, described in section 2.2.4, and the muon chambers are equipped instead with 3D Hall cards [31, 32]. These consist of a rigid printed-circuit board carrying a small glass cube, with a Hall probe on each of three orthogonal faces to measure each field component. Every card includes its own readout electronics, as well as a thermistor for local temperature compensation.

All the Hall cards were calibrated in a highly uniform field monitored by a NMR probe. The achieved absolute Hall-card accuracy on $|\mathbf{B}|$ is 0.2 mT up to $|\mathbf{B}| = 1.4$ T and 1 mT up to 2.5 T; and the angular accuracy achieved on the measured field direction is 2 mrad.

#### 2.2.3.2 B-field reconstruction

In an air-core magnet, the magnetic field can in principle be calculated by direct application of the Biot-Savart law, once the geometry of all conductors is known and assuming material-induced magnetic perturbations are negligible. In practice however, the conductor position and shape are known only approximately, owing to fabrication tolerances and to deformations of the magnet structure under gravitational and magnetic loads. The exact location of each magnet coil, as well as the relative positions of the end-cap and barrel toroids, will be reproducible, after a power cycle or an access period, to a finite precision only. Therefore, the field must be measured under running conditions, with all detector components in place and under the mutual influence of the different magnets and magnetic structures.

The muon spectrometer is equipped with an array of approximately 1730 Hall cards, which remain mounted permanently and precisely on the MDT chambers and continuously measure all three field components (an additional 64 cards are mounted on the inner and outermost faces of the end-cap toroid cryostats to complement the MDT sensor system in the forward region). Two NMR probes, installed at low-gradient locations in the barrel toroid, complement the system, with the aim of detecting eventual long-term drifts in the response of the Hall cards. The 3-D sensor readings are compared with field calculations which include both the contributions of the magnet windings and those of nearby magnetised structures, and are used for reconstructing the position and the shape of the toroid conductors with respect to the muon chambers (see figure 2.12). Once the geometry of the coils is known, the field can be calculated anywhere in the muon spectrometer. Simulation studies using a simplified coil deformation model have shown that the magnetic field can be reconstructed to a relative accuracy of 0.2% [27].

### 2.2.4 Solenoid-mapping measurements

#### 2.2.4.1 Mapping campaign

The field was mapped [33] in August 2006 by a machine, which scanned a Hall-card array over a volume slightly larger than that now occupied by the inner detector. During this mapping campaign, the barrel and end-cap calorimeters were all in their final positions. Although the shielding disks were not yet installed, their differential contribution is small enough ($< 0.2$ mT in the ID tracking volume) that it can be reliably accounted for later. The same is true of corrections for the absence of toroid excitation during mapping.



2008 JINST 3 S08003

Mapping data were recorded with solenoid currents of 7730, 7850, 7000, and 5000 A, with a final set of data back at the nominal operating current of 7730 A. Each data set contains at least 20,000 points, and is sufficient by itself to fit the field with negligible statistical uncertainty. Each map took about four hours, during which the solenoid current remained stable to within 0.1 A, as confirmed by the NMR probes.

#### 2.2.4.2 Mapper geometry, survey and auto-calibration

The mapping machine had four arms mounted on a common axle in a windmill configuration, with twelve Hall cards on each arm, at radii ranging from 0.118 to 1.058 m, which directly measured the field components $B_z$, $B_R$ and $B_\phi$. The machine could be rotated around its axle and translated in $z$ along the ID rails by means of pneumatic motors. Optical encoders allowed control of the mapper movements and readout of its stop positions with an accuracy of 0.1 mm. A number of surveys were necessary to determine the positions of each individual Hall sensor for all possible longitudinal mapper positions and azimuthal settings of the windmill arms. After combining all the information, the estimated overall accuracy on the position of a map point in the cryostat coordinate system is approximately 0.3 mm.

The redundancy and internal consistency of the mapping measurements makes it possible to extract individual probe misalignments from the data themselves to an accuracy of $\pm 0.1$ mrad. The strong constraints from Maxwell's equations on physically realisable fields in the absence of any current sources or magnetic materials, combined with the fact that the field at the origin can be almost completely determined from the measurements of a single Hall probe, allow all three probe alignment angles to be determined and the $B_z$ component to be normalised to a common scale for all probes.

The NMR probes, which were operational throughout the field-mapping campaigns, are used to set the overall scale of the Hall sensors with an accuracy of about 0.4 mT, the limitation coming from the extrapolation uncertainty from the mapper arms out to the position of the NMR probes. The NMR data also show that there is negligible hysteresis in the solenoid system: the field at 7730 A remained constant within $\pm 0.01$ mT from the first excitation cycle onwards, provided that this current was approached from below. A small saturation effect is visible in the NMR data, with the field at 5000 A being 0.34 mT higher than would be expected by simply scaling down from 7730 A.

#### 2.2.4.3 Map fitting

Using the measured magnet current and a detailed model of the solenoid geometry, the Biot-Savart law is integrated to produce a field model which should account for most of the measured field. The conductor model is based on engineering drawings, with as many parameters as possible taken from surveys of the as-built solenoid. The coil cross-section is assumed to be perfectly circular. The winding was mechanically assembled from four separate sections, each with a slightly different average pitch, and joined together by welds which are represented electrically by turns having just under twice the average pitch. Also modelled are the welds at the coil ends and the return conductor which runs axially along the outside of the support cylinder. The expected distortion

**Table 2.3**: Typical fit results of solenoid-mapping measurement at 7730 A.

| **Fitted parameters** | **Fit results** |
|---|---|
| Scale factors in conductor model | ($R$ scale, $z$ scale) = 0.9993, 1.0012 |
| Fitted offsets from solenoid centre to centre of cryostat | $(\Delta x, \Delta y, \Delta z)$ = 0.26, -2.42, 0.51 (mm) |
| Fitted rotations of solenoid around cryostat $x$ and $y$ axes | $(\theta_x, \theta_y)$ = -0.08, 0.19 (mrad) |
| Resulting fit residuals | $\sigma(\Delta B_z, \Delta B_R,\ \Delta B_\phi)$ = 0.44, 0.35, 0.30 (mT) |

of the solenoid, relative to the room-temperature survey and caused by thermal shrinkage and magnetic pressure, is also taken into account.

The geometrical fit to the mapping data has 11 free parameters. Two overall scale factors allow fine tuning of the conductor model: one common to all longitudinal dimensions, and an independent one for the radial dimension. Five more free parameters quantify the three offsets and two rotations of the conductor relative to the mapper coordinate system. The calorimeter-steel contribution is modelled by a Fourier-Bessel series with four terms. These parameters are determined by minimising a $\chi^2$ function which includes the longitudinal and radial field components at all mapped points. The RMS residuals of the geometrical fit alone are just over 0.5 mT. This field model is further improved by parametrising the difference between the data and the geometrical model with a general series which can represent any field obeying Maxwell's equations. This brings the residuals down to about 0.4 mT, as shown in table 2.3.

Systematic uncertainties are estimated by fitting to several representative data sets under varying assumptions, with and without implementing various corrections (such as Hall-card alignment, $z$-dependent carriage tilt, residual perturbations induced by slightly magnetic mapper components, number of Fourier-Bessel terms etc.). The geometrical scale factors emerge as very close to unity (table 2.3), suggesting that the coil survey data are well understood. The fitted offsets and rotations with respect to the centre of the reference coordinate system (barrel LAr cryostat) are stable at the 0.2 mm and 0.1 mrad level respectively, confirming the vertical -2 mm offset of the solenoid axis indicated by the survey results before and after installation in the main cavern (see table 9.2 in section 9.3.2.3).

The overall fit is excellent, as illustrated in figure 2.9 and confirmed by the resulting RMS residuals of $\sim$ 0.4 mT for all three field components (table 2.3). The on-axis fractional steel contribution, as estimated from the Fourier-Bessel series, is consistent with the magnetic-field simulation to better than 2 mT, although the latter does not perfectly reproduce the measured z-dependence of this perturbation. The fit quality is best measured in terms of the fractional sagitta residual, $\delta S/S$, evaluated along an infinite-momentum trajectory from the interaction point to the point where the track crosses the outer radial or longitudinal boundary of the inner detector. The total uncertainty, estimated by combining the overall scale error, the fit residuals and the systematic uncertainties, is shown as a function of $|\eta|$ in figure 2.13.

### 2.2.5 Experimental validation of the field map in the muon spectrometer

The tests carried out in fall 2006 for the barrel toroid provided the first full-scale test of the B-sensor system, and an initial validation of the magnetic models and field-reconstruction strategy in the muon spectrometer. The end-cap toroids were not yet installed at the time and the solenoid was



2008 JINST 3 S08003

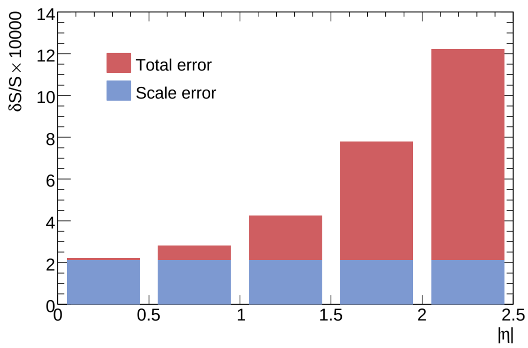


**Figure 2.13**: Fractional sagitta error due to uncertainties in the solenoid field vs. $|\eta|$.

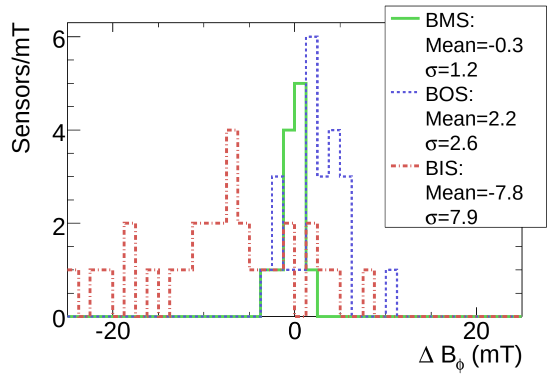


**Figure 2.14**: Field reconstruction residual $\Delta B_\phi$ for one middle (green, solid), outer (blue, dashed) and inner (red, dot-dashed) MDT layer.

turned off. Since the muon-chamber installation was still in progress, only 400 MDT Hall cards were available for readout, thus providing sensitivity for field reconstruction in about one third of the barrel region.

The sensor signals were extremely clean ($\sim 0.01$ mT of RMS noise at full field), and reproducible to $\sim 0.05$ mT between magnet cycles separated by up to one week. Non-linear effects remain very small ($< 4$ mT in the BIS layer, close to the calorimeter steel, over the full current range). The absolute field scale, as determined by an NMR probe located in the azimuthal mid-plane of coil 3, at a point where steel-induced perturbations are negligible and the field gradient below 0.2 mT/cm, agrees with the Biot-Savart prediction to better than 0.2%.

The field reconstruction algorithm outlined in section 2.2.3 and detailed in [27] has been applied to B-sensor data collected at nominal field in the barrel toroid. Because the muon alignment system was still being commissioned and the MDT survey not yet completed, it is necessary, at this stage, to assume that all muon chambers and B-sensors are in their nominal position. For the three coils bracketed by the available sensors, the reconstructed conductor shape is qualitatively consistent with that measured at room temperature before insertion of the windings into their respective cryostats. Figure 2.14 displays the difference, at each active sensor in sector 2 (see figure 6.1) of the muon spectrometer, between the azimuthal component of the measured field (corrected for perturbations from magnetic materials) and that of the Biot-Savart contribution predicted by the field-reconstruction fit. A perfect description of the conductor geometry and of magnetic perturbations should yield $\Delta B_\phi = 0$. The agreement is best in the middle chambers (BM), where the gradients are smallest: the distribution is well centred and exhibits a spread $\Delta B_\phi^{RMS} \sim 1.2$ mT. In the outer chamber layer (BOS), the distribution of $\Delta\, B_\phi$ shows a moderate bias of 2.2 mT and a spread of 2.6 mT. In view of the larger field gradient in these chambers, such a spread is consistent with the current $\pm 5$ mm uncertainty on the as-installed MDT chamber positions. The situation is similar but somewhat worse in the inner chambers (BIS). These preliminary results reflect the cumulative effect of errors in the assumed sensor and chamber geometry, of residual imperfections in the magnetic model of the calorimeter steel, and of the performance of the reconstruction fit.

Validation of the TOSCA simulations, which describe the distortions induced by other support and service structures was carried out using 40 dedicated Hall cards temporarily installed at critical locations in the bottom muon sector and between the outer muon chambers and the HS structure (see figure 2.11). The agreement between measured and predicted perturbations typically ranges from 2 to 5 mT at the location of the Hall cards and should be better within the spectrometer volume. It is satisfactory at most locations, although discrepancies as large as 50 mT are observed very close to a few localised and well-identified steel supports. A more extensive magnetic characterisation campaign is planned during the next full magnet-system test.

### 2.2.6 Towards an overall field map for ATLAS data-taking

The default field map in the ID tracking volume will mirror the very accurate fit obtained for the solenoid mapping data and illustrated in figure 2.9. This approach automatically takes into account the magnetised steel surrounding the ID cavity without having to rely on any field calculations. The fit function is required to satisfy Maxwell's equations and will include empirical corrections to match the measured map as closely as possible, as well as small ($< 0.2$ mT) additional corrections for the shielding disks (which were absent at the time of mapping) and barrel-toroid contributions.

In the calorimeters, the map will be based on the ATLM simulation, with the magnetic parameters describing the calorimeter steel adjusted to fit the solenoid-only and toroid-only field measurements performed in 2006. This simulated map will be smoothly connected to the fitted solenoid map in the future: the potential discontinuity remains to be characterised, but is estimated not to exceed 2 mT over a very narrow interface region.

In the muon spectrometer, the map will reflect the superposition of the winding contributions with the predicted distortions associated with the calorimeter steel and other significant magnetic structures inside or near the spectrometer volume. So far, the Biot-Savart calculation presented above has been performed only in a 1/16th slice, which spans 45° in azimuth and is longitudinally symmetric with respect to the interaction point: this is the minimum angular size required to handle correctly the symmetries of the full toroid system. Extending it to the case of an arbitrary geometry (without any symmetry assumptions) is currently in progress and the final implementation will depend on the extent to which the actual coil geometry, as eventually revealed by the field-reconstruction procedure, deviates from the ideal configuration. Similarly, studies are in progress to assess the magnetic impact of shape or position imperfections in the tile-calorimeter geometry: their outcome will indicate to which extent such deviations from the ideal configuration must be taken into account when describing the field inside the calorimeter and/or muon spectrometer.



2008 JINST 3 S08003